Multi-MeV Electron Beam Generation by Direct Laser Acceleration in High-Density Plasma Channels

C. Gahn,[1] G. D. Tsakiris,[1] A. Pukhov,[1] J. Meyer-ter-Vehn,[1] G. Pretzler,[1] P. Thirolf,[2] D. Habs,[2] and K. J. Witte[1]
[1]*Max-Planck-Institut für Quantenoptik, D-85748 Garching, Germany*
[2]*Sektion Physik, LMU München, Am Coulombwall 1, D-85748 Garching, Germany*
(Received 17 June 1999)

We have measured angularly resolved and absolutely calibrated spectra of the multi-MeV electrons produced by relativistic self-channeling in a high-density gas jet. Using 200 fs laser pulses with $P_L = 1.2$ TW, we have investigated the electron spectrum dependence on the plasma electron density in the range of $3 \times 10^{19}-4 \times 10^{20}$ cm^{-3}. The experimentally obtained results are closely reproduced by three-dimensional particle-in-cell simulations. A detailed analysis shows that the self-modulated laser wake field, although active, cannot explain the experimental energy spectrum. The bulk of the fast electrons are produced by direct laser acceleration at the channel betatron resonance.

PACS numbers: 52.40.Nk, 52.60.+h, 52.70.Nc, 52.75.Di

Present-day high-power laser systems can produce ultrashort pulses [1] with intensities well above 10^{18} W/cm^2. In plasma, they are subject to relativistic self-channeling [2–8], when exceeding the power $P_{\mathrm{RSF}} \approx 17(n_c/n_e)$ GW. Here n_e is the plasma electron density and n_c is the critical density, $n_c = 1.7 \times 10^{21}$ cm^{-3} for a laser wavelength of 0.8 μm. Experiments [9–15] and particle-in-cell (PIC) simulations [16,17] show that the relativistic self-channeling of laser pulses is accompanied by electron acceleration to multi-MeV energies that are ejected as a low-emittance beam in the direction of laser propagation [12]. A number of potential applications has been envisaged for these electrons ranging from the "fast ignitor" concept for inertial confinement fusion [18] to laser induced nuclear reactions [19].

One of the central issues in this Letter is to pinpoint the mechanism of electron acceleration in relativistic laser channels. The analysis is based on PIC simulations which are in detailed agreement with new high-quality experimental data presented here. The measured electron energy spectra, resolved in angle and absolutely calibrated, pertain to electron acceleration during self-channeling in a previously unexplored regime, characterized by fs-laser pulses of relatively *low energy* (<1 J) interacting with a *high-density* ($n_e \sim 0.2n_c$) gas jet. The numerical part is based on direct full-scale three-dimensional particle-in-cell (3D PIC) simulations [17] using the code Virtual Laser Plasma Lab (VLPL) [20]. It treats the experiment in real geometry and uses the experimental profiles of laser pulse and target density. Previous simulations of relativistic laser plasma interaction have used 2D PIC simulation [16] or 3D simulations in the envelope approximation with ponderomotive description of electron motion [21,22].

Because the process of self-focusing is known to be strongly geometry dependent [23], 3D geometry is a crucial point. When exceeding the threshold in realistic 3D geometry, the electromagnetic wave abruptly shrinks down to the nonlinear saturation limit set by electron cavitation [4], while it contracts more gradually in 2D planar geometry, allowing for stable beam propagation even without electron cavitation. Also, 2D results strongly depend on laser ($s-$ or $p-$) polarization, a feature absent in experiment and 3D treatment. Concerning the ponderomotive description of relativistic electrons, it has been shown to fail in [24] when the laser beam focuses down to a narrow spot. The present 3D PIC simulations therefore represent significant progress.

In our 3D PIC simulations, we trace all electrons to identify the origin of energy gain. The results suggest that the electrons experience direct laser acceleration (DLA) at the channel betatron resonance as first described by Pukhov *et al.* [25]. The mechanism [25] is similar to that of inverse free electron lasers [26], where the wiggler field is replaced by the self-generated quasistatic electric and magnetic fields in the channel [17,27]. The relativistic electrons make transverse oscillations at the betatron frequency $\omega_\beta \approx \omega_p/(2\gamma)^{1/2}$ in these fields while drifting along the channel together with the light. Here, γ is the relativistic γ factor and $\omega_p = 4\pi e^2 n_e/m_e$ is the plasma frequency. When ω_β coincides with the laser frequency as observed by the relativistic electron, the channel resonance results in effective energy exchange between laser wave and electron. Energy gain from longitudinal plasma waves, pertinent to forward Raman scattering or self-modulated laser wake-field acceleration [21] and considered as the dominant mechanism in previous experiments at lower density [9,12,13,15], plays only a minor role in our experiment. Another way of DLA, mediated by transverse stochastic perturbations, has been considered in [28], and acceleration by the longitudinal electric field of a focused laser beam is discussed in [29].

The experiment was performed with the Advanced Ti:sapphire Laser (ATLAS) at Max–Planck–Institut für Quantenoptik that delivers 200-fs, 250-mJ pulses at 790 nm. The laser beam was focused with an f/3 off-axis parabolic mirror to a spot of 15 μm in diameter

 0031-9007/99/83(23)/4772(4)$15.00

containing 85% of the total energy with peak intensity of 4×10^{18} W/cm^2. The focus was placed at the edge of a free expansion helium gas jet generated by a high pressure gas nozzle with a circular orifice of 500 μm in diameter [7]. The transverse density profile in the interaction region 100 μm away from the nozzle tip corresponds to a Gaussian profile with half the peak density at the edge of the orifice. The electron density in the tunnel-ionized underdense plasma created by the foot of the laser pulse is linearly proportional to the backing pressure up to a maximum value of 4×10^{20} cm^{-3}.

In order to diagnose self-focusing and channel formation, a side-scattering imaging system at 90° to the laser beam direction was utilized. Using an interference filter this system took self-scattered time integrated images of the radiation at the fundamental laser wavelength with a spatial resolution of 5 μm.

Two different diagnostics for electron detection were employed. The first one consisted of a phosphorescent screen placed behind a 100-μm-thick aluminum foil that blocked the laser light and electrons with energies less than 200 keV. The purpose of this device was to visualize the relativistic electrons and qualitatively optimize their production. At an electron density of 3×10^{19} cm^{-3} a faint round spot appeared on the screen centered on the laser axis and it became brighter at higher densities. When a static magnetic field of 1 kG was applied between filter and screen, this spot moved in the direction expected for a beam of electrons. The main electron diagnostic was a compact 45-channel magnetic spectrometer [30], which after beam optimization replaced the filter and screen and with which quantitative measurements of the electron energy distribution in a range from 500 keV up to 12.5 MeV were performed. The electrons were collimated by an aperture located 14 cm away from the laser focus, dispersed by a permanent dipole magnet and finally detected by scintillating/light-guiding plastic fibers which were coupled via a fiber optics to a cooled charge-coupled device camera. The spectrometer was absolutely calibrated using various β emitters and it was rotated horizontally as well as vertically around the interaction region up to an angle of 10° relative to the laser beam direction thus allowing measurements of the angular distribution of the relativistic electrons.

A typical energy spectrum that was measured in laser beam direction (from now on denoted by 0°) at an electron density of 2×10^{20} cm^{-3} is shown in Fig. 1. It follows a Boltzmann-like distribution with an effective temperature of 5 MeV and extends to 12.5 MeV which was the spectrometer limit.

The total number of electrons and their effective temperature for different electron densities were determined by rotating the spectrometer and, hence, scanning the beam in steps of 2.5° in the horizontal plane. The spectra integrated over the solid angle are shown in Fig. 2.

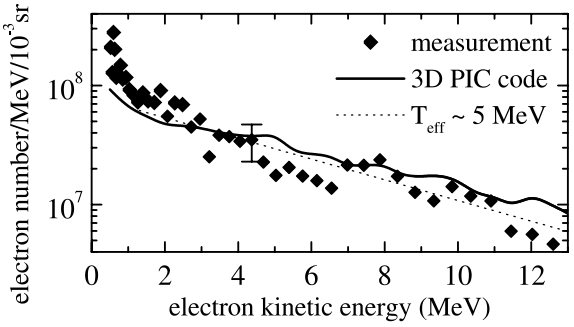

FIG. 1. Typical electron spectrum measured in laser beam direction (diamonds) and exponential fit (dotted line). The prediction of the 3D PIC simulations is also shown (solid line).

As the density is increased, relativistic electrons appear at 3×10^{19} cm^{-3} just above the threshold for self-focusing as can be seen from Fig. 3. Here the observed channel lengths for the different densities are compared to the confocal parameter (twice the Rayleigh length $2z_R$) which is about 70 μm. When the density is increased to 5×10^{19} cm^{-3}, a self-focused channel of 220 μm is observed and the temperature of the fast electrons rises strikingly from 300 keV to 1 MeV measured at 0°. Since the outer parts of the beam are somewhat "colder," the angle averaged temperature is 600 keV as shown in Fig. 2. Further increasing the density leads to a maximum temperature of 3.3 MeV at a density of 2×10^{20} cm^{-3} and simultaneously to the longest channel of almost 400 μm. The total number of MeV electrons amounts to 2×10^{10}, which corresponds to a conversion efficiency of laser energy into collimated electron energy of 5%.

As the plasma density increases, the self-focusing power threshold drops, and the effective ratio P/P_{RSF} rises. A larger portion of the laser beam is trapped in the channel and its length grows. At the plasma density of $n_e = 2 \times 10^{20}$ cm^{-3} we observe an optimum at which

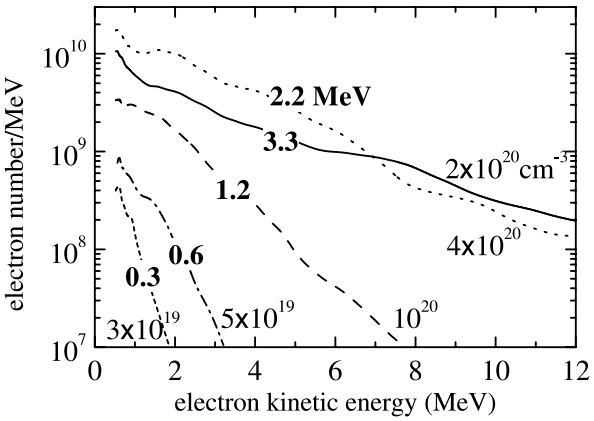

FIG. 2. Experimentally determined electron-spectrum dependence on different electron densities (labeled by normal letters). Bold letters give the effective temperatures of the (not shown) exponential fits.

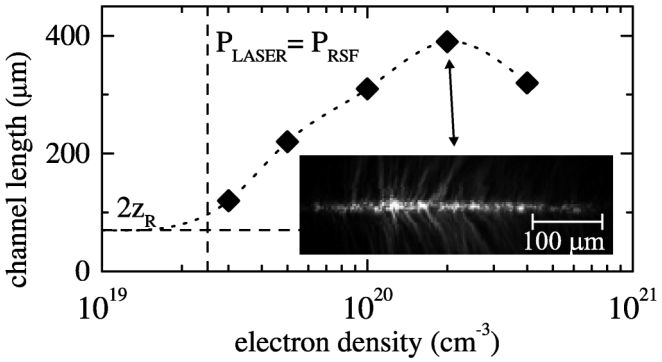

FIG. 3. Dependence of channel length on plasma density (diamonds are the experimental data and the dotted line is to guide the eye). The vertical dashed line shows the theoretical threshold for relativistic self-focusing. Inset: Image of the longest measured channel.

most of the laser energy is trapped in the channel. This optimal plasma density is set by the laser pulse parameters. Both channel length and effective temperature of fast electrons are maximized here. At the highest density that could be achieved with this experimental setup, namely 4×10^{20} cm^{-3}, the number of electrons still increases, but the temperature as well as the channel length decrease again. This is attributed to higher energy losses due to electron heating. Losses to ionization and ionization defocusing [7] occur at the channel boundaries, but play no role in the channel center, where electron trapping and acceleration takes place.

The hottest electron spectrum at the density of 2×10^{20} cm^{-3} is made up of a hot component of 5 MeV in the center of the beam measured at 0° and colder components in the outer parts, namely, 4 MeV at 5° and finally 2 MeV at 10°. This indicates that the very fast electrons with energies exceeding 10 MeV are more collimated than the less energetic ones. Figure 4 depicts this behavior. Here, the angular spread of electrons in three different energy ranges is shown. It diminishes from 16° FWHM (full width at half maximum) for 3-MeV electrons to 9° for 11-MeV electrons. Within the accuracy of the measurements, the electron beam appears to be azimuthally symmetric.

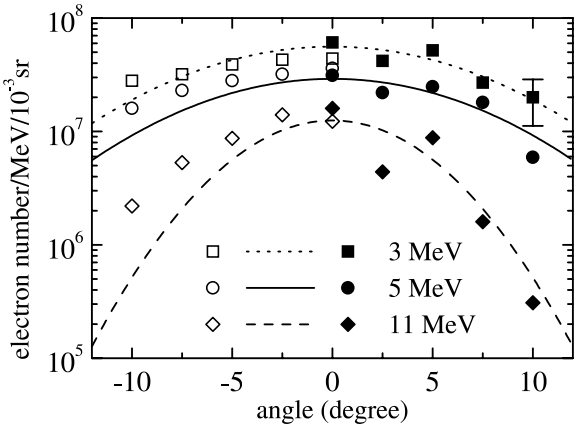

FIG. 4. Angular dependence of electrons with different energies. Solid symbols are experimental data, lines are Gaussian fits to the data, and hollow symbols are results from 3D PIC simulations.

Figures 1 and 4 suggest that the 3D PIC simulations reproduce the experimental measurements dependably not only in form but also in absolute numbers. We should emphasize here that the 3D capability of the code allows us to simulate closely the experimental conditions including laser and density profile. This results in *absolute* energy spectra, i.e., the number of accelerated electrons in an energy range in a solid angle cone. We now analyze the simulation results in more detail to identify the dominant mechanism of electron acceleration.

Having the full information about the electron dynamics in the PIC simulation, we separate the two driving terms in the equation of motion $dp^2/dt = -2eE_z p_z - 2e\vec{E}_\perp \cdot \vec{p}_\perp$ with $\vec{E}_\perp \cdot \vec{p}_\perp = E_x p_x + E_y p_y$, keeping track of

$$\Gamma_z = -\int_0^t \frac{2eE_z p_z}{(mc)^2}\, dt, \qquad \Gamma_\perp = -\int_0^t \frac{2e\vec{E}_\perp \cdot \vec{p}_\perp}{(mc)^2}\, dt, \tag{1}$$

in the energy $\gamma^2 = 1 + (p/mc)^2 = 1 + \Gamma_z + \Gamma_\perp$ of each electron. Here, Γ_z is the energy gain at time t due to acceleration by the longitudinal electric field E_z mainly representing the plasma wave (wake field), while $\Gamma_\perp$ represents direct laser acceleration by the transverse field $E_\perp$. The contribution of the transverse electrostatic channel field averages to zero in $\Gamma_\perp$. Notice that the relativistic electrons are mainly moving in a forward direction along the channel axis, while oscillating transversely and gaining energy from the laser electric field ($p_z \gg p_\perp \gg mc$); increments of $p_\perp$ are then converted into increments of p_z via $\vec{v} \times \vec{B}$ interaction.

We consider the case for the optimal experimental parameters, $n_e = 2 \times 10^{20}$ cm^{-3}, corresponding to electrons generated with highest energy. The results of PIC simulations are shown in Figs. 5a–5h. The snapshot is taken when the head of the laser pulse has just arrived at the maximum plasma density in the gas jet, $z = 300\lambda$. The regular wake field exists at the head of the laser pulse only (Fig. 5a), causing strong modulations with plasma period in phase space (Fig. 5b–5d). Nevertheless, the comparison between Γ_z and $\Gamma_\perp$ in Figs. 5e–5f reveals that most of the energy acquired is due to direct laser acceleration, while laser wake field acceleration (LWFA) drives only a minority of electrons. Actually, most electrons experience a net drag from the wake field ($\Gamma_z < 0$ in Fig. 5e). Figure 6a, where electrons are plotted in the (Γ_z, $\Gamma_\perp$) plane, clearly exhibits this feature. All electrons are located in the half-space $\gamma^2 = 1 + \Gamma_z + \Gamma_\perp > 1$ with the bulk in the quadrant $\Gamma_z < 0$, $\Gamma_\perp > 0$, giving clear evidence that DLA is the dominant acceleration mechanism and that

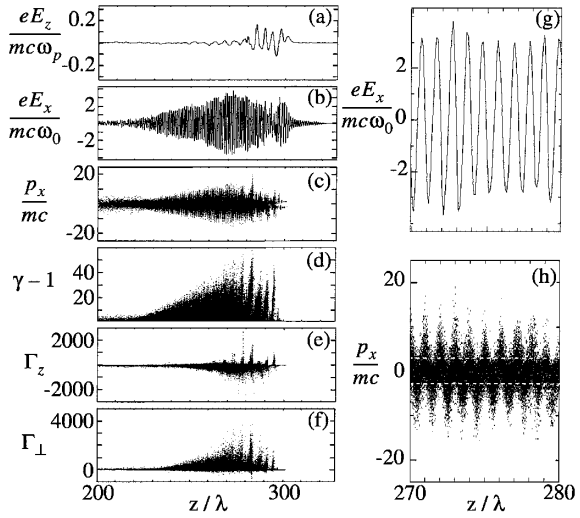

FIG. 5. 3D PIC simulations. The frames show the following: (a) the wake field $eE_z/mc\omega_p$; (b) the laser field $eE_x/mc\omega_0$, where ω_0 is the *laser* frequency; (c) the transverse momentum p_x/mc; (d) the electron energy distribution $\gamma - 1$; (e) the gain Γ_z; (f) the transverse gain $\Gamma_\perp$; all along the laser propagation axis z. Zoom at $270 < z/\lambda < 280$ of (g) $eE_x/mc\omega_0$ and (h) p_x/mc with the dashed line indicating $|p_x/mc| = 3$.

LWFA decelerates rather than accelerates electrons. Sorting electrons of given energy into groups of $\Gamma_z > \Gamma_\perp$ (LWFA dominant) and $\Gamma_z < \Gamma_\perp$ (DLA dominant) leads to the spectra in Fig. 6b. It demonstrates that LWFA plays only a minor role in the present experiment.

Finally, a closer look into the transverse electron dynamics is given in Figs. 5g–5h, where the z axis has been expanded to laser wavelength resolution. Notice that the laser amplitude $a = eE_x/mc\omega_0 = 3.0$ in the self-focused channel is larger than the value $a = 1.7$ of the incident pulse and that the transverse momenta of many electrons exceed $a = 3$ significantly, i.e., $p_x/mc \gg 3$. The reason for this is resonant energy transfer from the laser wave to electrons performing transverse oscillations in the channel at the betatron frequency. The theory

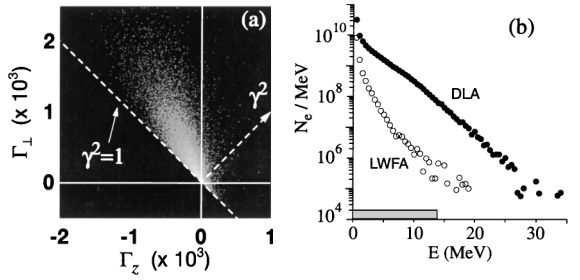

FIG. 6. Breakdown of electron spectrum with respect to the major acceleration mechanism. (a) Distribution of the accelerated electrons in the $(\Gamma_z, \Gamma_\perp)$ space. The shaded histogram is in logarithmic scale. (b) The filled circles represent the DLA spectrum of electrons while the empty circles mark the LWFA spectrum. The bar at the energy axis marks the range of the electron detector used in the experiment (see text for details).

explaining the quasithermal form of the spectra has still to be worked out.

In conclusion, we have performed a detailed experimental characterization of multi-MeV electrons accelerated by the 1.2-TW ATLAS laser pulse channeling in a high-density gas jet. The angularly resolved electron energy spectra calibrated in absolute numbers are closely reproduced by 3D PIC simulations with the VLPL code. In the PIC simulations, we were able to separate contributions from the plasma wake field and the laser electric field itself. For the present experiment at high plasma density, we find direct laser acceleration to be the dominant process. We have checked that this result remains valid also for lower densities as long as a self-focusing channel is formed trapping laser power $P \gg P_{\mathrm{RSF}}$.

This research was supported by the Commission of the EC within the framework of the Association Euratom—Max-Planck-Institut für Plasmaphysik and DFG Contract No. Ha 1101/7-1. The technical assistance of H. Haas and A. Böswald is greatly appreciated.

[1] G. A. Mourou *et al.*, Phys. Today **51**, No. 1, 22 (1998).
[2] C. E. Max *et al.*, Phys. Rev. Lett. **33**, 209 (1974).
[3] P. Sprangle *et al.*, IEEE Trans. Plasma Sci. **15**, 145 (1987).
[4] G.-Z. Sun *et al.*, Phys. Fluids **30**, 526 (1987).
[5] P. Monot *et al.*, Phys. Rev. Lett. **74**, 2953 (1995).
[6] M. Borghesi *et al.*, Phys. Rev. Lett. **78**, 879 (1997).
[7] R. Fedosejevs *et al.*, Phys. Rev. E **56**, 4615 (1997).
[8] K. Krushelnick *et al.*, Phys. Rev. Lett. **78**, 4047 (1997).
[9] A. Modena *et al.*, Nature (London) **377**, 606 (1995).
[10] D. Umstadter *et al.*, Science **273**, 472 (1996).
[11] G. Malka *et al.*, Phys. Rev. Lett. **79**, 2053 (1997).
[12] R. Wagner *et al.*, Phys. Rev. Lett. **78**, 3125 (1997).
[13] C. I. Moore *et al.*, Phys. Rev. Lett. **79**, 3909 (1997).
[14] X. F. Wang *et al.*, Opt. Commun. **146**, 363 (1998).
[15] D. Gordon *et al.*, Phys. Rev. Lett. **80**, 2133 (1998).
[16] K. C. Tzeng *et al.*, Phys. Plasmas **6**, 2105 (1999).
[17] A. Pukhov and J. Meyer-ter-Vehn, Phys. Rev. Lett. **76**, 3975 (1996); Phys. Plasmas **5**, 1880 (1998).
[18] M. Tabak *et al.*, Phys. Plasmas **1**, 1626 (1994).
[19] P. L. Shkolnikov *et al.*, Appl. Phys. Lett. **71**, 3471 (1997); S. Karsch *et al.* (to be published).
[20] A. Pukhov, J. Plasma Phys. **61**, 425 (1999).
[21] E. Esarey *et al.*, Phys. Rev. Lett. **72**, 2887 (1994).
[22] P. Chessa *et al.*, Phys. Plasmas **5**, 3451 (1998).
[23] A. Schmitt, Phys. Fluids **31**, 3079 (1988).
[24] B. Quesnel and P. Mora, Phys. Rev. E **58**, 3719 (1998).
[25] A. Pukhov *et al.*, Phys. Plasmas **6**, 2847 (1999).
[26] E. D. Courant *et al.*, Phys. Rev. A **32**, 2813 (1985); M. P. Pato *et al.*, Nucl. Instrum. Methods Phys. Res., Sect. A **238**, 342 (1993).
[27] M. Borghesi *et al.*, Phys. Rev. Lett. **80**, 5137 (1998).
[28] J. Meyer-ter-Vehn and Zh. M. Sheng, Phys. Plasmas **6**, 641 (1999).
[29] S. Wilks *et al.*, Rutherford Appleton Lab, Oxford, RAL-TR-1998-085 (1998).
[30] C. Gahn *et al.* (to be published).